

# Molecular beam study of the chemiluminescent reaction of manganese and ozone

K. M. Green, R. P. Kampf, and J. M. Parson<sup>a)</sup>

*Department of Chemistry, The Ohio State University, 100 W. 18th Avenue, Columbus, Ohio 43210*

(Received 14 September 1999; accepted 27 October 1999)

The electronically chemiluminescent reaction  $\text{Mn} + \text{O}_3 \rightarrow \text{MnO}^* + \text{O}_2$  was investigated using a beam-gas configuration. Light from the  $\text{MnO } A \ ^6\Sigma^+ - X \ ^6\Sigma^+$  transition was collected by a charge coupled device (CCD) array detector with resolutions of 0.5 and 0.1 nm. The spectrum at lower resolution (500–655 nm) encompassed the  $\Delta v = -3$  to  $+2$  sequences, while that at higher resolution (555.5–583.5 nm) encompassed only the  $\Delta v = 0$  sequence. These two spectra were separately fitted with a nonlinear least-squares program to obtain vibrational and rotational distributions of the nascent  $\text{MnO}^*$ . The limited vibrational-state coverage of the higher-resolution spectrum made it unreliable for determining the vibrational state distribution, and it was useful only for characterizing the rotational distribution when  $v' = 0$ . The best-fit vibrational excitation is somewhat less than for the Prior model, but the rotational excitation is considerably greater. A consideration of the electronic structure of reactants and products indicates that principal changes occurring in the chemiluminescent reaction are  $\sigma$ -electron donation from the  $sd_{z^2}$  hybridized Mn orbital to the  $\text{O}_3$  lowest unoccupied molecular orbital (LUMO) ( $2b_1$ ) and  $\pi$ -electron backdonation from the  $\text{O}-\text{O } 4b_2$  orbital to the  $\text{Mn } 3d_{\pi}$  orbital. Correlation of the orbitals involved indicates that direct access is allowed to the  $\text{MnO } A \ ^6\Sigma^+ (10\sigma^*18\sigma^1)$  state. This mechanism favors Mn approach perpendicular to the  $\text{O}_3$  plane and suggests that the product's rotational excitation may originate in  $\text{O}_2$ -OMn repulsion arising from removal of electron density from the slightly bonding  $4b_2$  orbital of  $\text{O}_3$ . However, some rotational excitation could also be attributed to conservation of angular momentum arising from a sizable reactive impact parameter. The lack of significant vibrational excitation is a consequence of the short-range nature of the partial charge transfer in this reaction channel. © 2000 American Institute of Physics. [S0021-9606(00)01204-6]

## I. INTRODUCTION

The chemistry of transition metal compounds is most frequently studied and utilized in condensed phases where the transition metal is encumbered with ligands. Although a detailed understanding of reaction pathways is critical in developing catalysts and dealing with many enzymatic reactions, prospects for accurate *ab initio* calculations of stable species or reaction intermediates in these environments remain dim, particularly because of the extra challenges of dealing with unpaired *d*-electrons and relativistic effects. So, the fairly recent surge of interest in gas-phase reactions of free transition metal atoms and ions by experimentalists and theorists alike can be thought of as providing a basis for eventually handling more practical chemistry in solutions or at gas/surface interfaces, rather than a movement to make catalytic chemistry practical in the gas phase. Previous work on reactions which form transition metal oxides has concentrated on the early groups, which form very strong monoxides. For the middle groups, the monoxide bond is often weaker than the dioxygen bond, and we turn to ozone as an oxidizing gas since it has a very weak  $\text{O}_2$ -O bond strength of 1.1 eV, and offers the potential of forming metal dioxides in a single step. As in our previous work, a high-temperature oven was used to generate an effusive metal beam, which

collided with the oxidizing gas under single-collision conditions. The details of the elementary reaction step, which in this case was formation of electronically excited MnO, could be inferred by analyzing the emission spectrum. Further insight could be gained by studying the process as a function of collision energy. This study did not concern MnO formation in the ground electronic state, which may be the predominant reaction.

It is essential in this type of dynamics study to have the spectroscopy of the observed molecules well understood at the outset. Like most transition metal diatomics, MnO has many possible electronic states and a history of disputed assignments. By 1975,<sup>1</sup> though, the  $A-X$  transition which we have observed was well-accepted as  $^6\Sigma^+ - ^6\Sigma^+$ , and can be understood as arising from a charge transfer between the  $10\sigma^*$  and  $8\sigma$  molecular orbitals,<sup>2</sup> which make use of  $sd_{z^2}$ -hybrid orbitals<sup>3-5</sup> of Mn and the  $2p_z$  orbital of O. The values of the spectroscopic constants needed for a computer simulation of the spectrum are given in Table I. The boldface parameters form a consistent set which was used in the simulation.

The current work appears to be the first report of Mn reacting with ozone under single-collision conditions. Gole and co-workers did report emission spectra of Mn clusters with ozone under multiple-collision conditions,<sup>6,7</sup> where Mn

<sup>a)</sup>Electronic mail: parson.2@osu.edu

TABLE I. Summary of MnO spectroscopic constants.

MnO	Spectroscopic constant	$A \text{ } ^6\Sigma^+$	$X \text{ } ^6\Sigma^+$
Electronic	$T_e, \text{ cm}^{-1}$	17 949 <sup>a</sup> <b>17 943<sup>b</sup></b> 17 894 <sup>d</sup>	<b>0</b>
	$D_0^0 \text{ eV}$	<b>3.78</b> (calc)	<b>3.70<sup>b</sup></b> 3.82 <sup>c</sup>
Vibrational	$\omega_e, \text{ cm}^{-1}$	<b>762.8<sup>a</sup></b>	839.6 <sup>a,b</sup>
	$\omega_e x_e, \text{ cm}^{-1}$	<b>9.6<sup>a</sup></b>	4.79 <sup>a,b</sup>
	$\omega_e y_e, \text{ cm}^{-1}$	<b>0.06<sup>a</sup></b>	...
Rotational	$B_e, \text{ cm}^{-1}$	0.390 <sup>a</sup> <b>0.4651<sup>b</sup></b> 0.45 885 ( $\nu=1$ ) <sup>d</sup>	0.435 <sup>a</sup> <b>0.50 325<sup>b</sup></b>
	$\alpha_e, \text{ cm}^{-1}$	<b>0.0036<sup>b</sup></b>	<b>0.00 406<sup>b,d</sup></b>
	$R_e, \text{ \AA}$	1.868 <sup>a</sup> <b>1.7107<sup>b</sup></b>	1.769 <sup>a</sup> <b>1.6458<sup>b</sup></b>
	$D_e, \text{ cm}^{-1}$	<b><math>2.04 \times 10^{-6b}</math></b>	<b><math>7.2 \times 10^{-7b}</math></b>
	$\beta_e, \text{ cm}^{-1}$	...	<b><math>6.0 \times 10^{-9b}</math></b>
Spin-spin	$\lambda, \text{ cm}^{-1}$	0 <sup>a</sup> <b>0.43<sup>b</sup></b> -0.13 <sup>d</sup> -0.104 ( $\nu=1$ ) <sup>d</sup>	0.66 <sup>a</sup> <b>1.13<sup>b</sup></b> 0.57 <sup>d</sup> 0.574 ( $\nu=0$ ) <sup>d</sup>
	$\gamma, \text{ cm}^{-1}$	<b>-0.0021<sup>b</sup></b> 0.0017 ( $\nu=1$ ) <sup>d</sup>	<b>-0.0019<sup>b</sup></b> -0.003 <sup>d</sup> -0.0024 ( $\nu=0$ ) <sup>d</sup>

<sup>a</sup>From Ref. 10. This reference cites  $D_0^0$  from  $b$  and  $e$ , and spectroscopic constants from Ref. 29.

<sup>b</sup>Reference 82.

<sup>c</sup>Reference 83. This value was used for calculating the reaction exothermicity.

<sup>d</sup>Reference 84.

and its clusters were entrained in the inert gas. Levy and co-workers observed chemiluminescent reactions of laser-vaporized Mn atoms with  $\text{N}_2\text{O}$  (Ref. 8) and  $\text{O}_2$ ,<sup>9,10</sup> at much higher collision energies than were used in this study. They concentrated on the collision-energy dependence of the cross section, rather than the spectrum of the products.

## II. EXPERIMENTAL APPARATUS AND PROCEDURES

The apparatus and techniques used to produce the spectra and reagent ozone have been previously described in detail elsewhere.<sup>11,12</sup> Manganese atoms were vaporized from a tantalum crucible at oven temperatures around 1253 K (9.9 mTorr Mn). A commercial ozonator (Ozoteq model 25-0) was used to generate a flow of ozone from dry  $\text{O}_2$ . Since pure ozone was needed, this flow was introduced into a glass flask cooled in a dry ice/isopropanol bath, where the ozone was selectively adsorbed to freshly dried silica gel. When sufficient ozone had accumulated, the  $\text{O}_2$  was pumped away, and ozone was leaked through a glass/Teflon needle valve into the vacuum chamber. Ozone pressures were typically maintained at about 0.2 mTorr.

The green chemiluminescence (CL) was recorded in first order with a 0.75 m scanning monochromator (Spex model 1702) equipped with either a 300 or 1200 lines/mm grating which had been converted in-house to a polychromator with a CCD detector replacing the exit slit. The widths of the entrance slit used were, respectively, 0.125 and 0.100 mm.

The liquid-nitrogen-cooled, front-illuminated 1152×256 pixel CCD array (Princeton Instruments model LN/CCD-1152-UV) was used to obtain the raw spectra. This model is coated with a UV-vis converting material to extend the effective range of detection down to 180 nm. The CCD array was installed so that the CL was dispersed across the 1152 pixel width for maximum resolution. On-chip binning was performed along the 256 pixel width for lower readout noise.

Initial processing of the spectra included filtering to remove spurious peaks, eliminating the background and calibrating both the wavelength and the relative intensity.<sup>13,14</sup> Adjacent frames were overlapped so that they could be scaled to agree in the regions of overlap. Spurious peaks arose principally from cosmic rays and were removed with a derivative filter supplied by the manufacturer. By averaging multiple scans of the same spectral region after removing the cosmic rays, the signal-to-noise ratio was improved. The background signal arising from oven light and readout bias was subtracted from the total signal for each pixel. CCD pixel number was calibrated against the known positions of atomic lines emitted by a mercury lamp, according to methods previously given.<sup>11</sup> The spectrum was corrected for spectral response by measuring the output of a standard quartz-halogen lamp (for wavelengths longer than 400 nm). After these steps were taken, the best approximation of the true spectrum was input into a simulation program.

A separate time-of-flight (TOF) collision chamber, which has been described earlier,<sup>11,12</sup> was used to obtain the dependence of the CL signal on the Mn velocity. A rotating slotted wheel provided Mn pulses of 21  $\mu\text{s}$  duration. The beam flight path was 18.3 cm and the region of observed CL was 1 cm long, inside of a liquid-nitrogen-cooled cell containing the ozone. Cooling the ozone served to narrow the range of relative collision velocities for each Mn velocity sampled. The Mn source temperature was chosen to be low enough (1270 K, yielding 14 mTorr) to assure that the velocity distribution was Maxwellian. The ozone pressure in the cell was approximately 0.5 mTorr. TOF curves were simulated using various forms for the collision energy dependence of the CL cross section having adjustable parameters. The simulations, which were fit to the experimental spectra with a nonlinear least-squares routine,<sup>15</sup> used the relative velocity distributions resulting from the ozone and Mn Maxwell-Boltzmann velocity distributions<sup>16</sup> and also accounted for the temporal and spatial widths of the beam pulse and observation zone.

## III. SPECTRAL SIMULATIONS

As its source, the intensity of a spectral line emitted from level  $i$  to level  $f$  is<sup>17</sup>

$$I(i,f) = h\nu_{i \rightarrow f} N(i) A(i,f), \quad (1)$$

where the Einstein  $A$ -coefficient  $A(i,f)$  and the line strength  $S(i,f)$  are defined in Eq. (2):

$$A(i,f) = \frac{64\pi^4\nu_{i\rightarrow f}^3}{3h} \sum_{m_i} \sum_{m_f} |\langle m_i | \hat{P} | m_f \rangle|^2$$

$$= \frac{64\pi^4\nu_{i\rightarrow f}^3}{3h} S(i,f). \quad (2)$$

$\hat{P}$  is the electric dipole, and  $\langle m_i |$  and  $| m_f \rangle$  are the wave functions for the initial and final states, respectively.

To gain information on the detailed reactive cross section, the source intensity for CL must be expressed in terms of the reactive flux for formation of state  $i$ ,  $F(i)$ . Assuming state  $i$  achieves a steady-state concentration, the reactive flux of formation of  $i$  will then be the same as the net flux of  $i$  being lost from the detector. The main processes through which state  $i$  can be lost are by (i) radiative relaxation to any lower state, (ii) diffusion out of the detection volume, and (iii) collisional deactivation.<sup>18</sup> The experiment was done under single-collision conditions, making collisional deactivation improbable. The rate for diffusion out of the detection volume is at least one order of magnitude slower ( $1/\tau_{\text{diff}} \leq 10^6 \text{ s}^{-1}$ ) than the radiation rate ( $1/\tau_{\text{rad}} \geq 10^7 \text{ s}^{-1}$ ). Consequently, the net flux of  $i$  being lost can be approximated by the radiative flux out of bright state  $i$  to all possible dark states  $f$ ,<sup>19</sup> i.e., by the CL from state  $i$ ,

$$I_{\text{CL}}(i) = \frac{N(i)}{g_i} \sum_f h\nu_{i\rightarrow f} A(i,f). \quad (3)$$

Several further assumptions were made concerning the flux out of the nascent chemiluminescent level. The flux depends on the populations in the nascent chemiluminescent level characterized by both the vibrational and rotational quantum numbers. This is represented by  $P(v', J')$ . To make this distribution of states more manageable, we first made the approximation that this joint rovibrational distribution,  $P(v', J')$ , is composed of two distinct, independent distributions:<sup>20</sup> the vibrational distribution  $P(v')$  and the rotational distribution  $P_{v'}(J')$ . In other words,<sup>21</sup>

$$N(i) \propto P(v', J') = P(v') P_{v'}(J'), \quad (4)$$

where  $P(v')$  and  $P_{v'}(J')$  are normalized over  $v'$  and  $J'$ , respectively. Second, due to the large number of degrees of freedom and to avoid scatter in the calculated distributions,<sup>22</sup> these separate populations were approximated by flexible parametric functions. Several different functional models were examined. The actual forms used to achieve the best fit will be presented later, along with the results.

Since the transition is between  $\Sigma$  states, it is reasonable to assume that in the rotating molecule, for low rotational speeds, wave functions are well-represented as pure Hund's case (b):  $|e v\rangle | \Lambda S \Sigma; \Omega J M \rangle$ . [In this case the main rotational energy is given by the rigid rotor expression in terms of the rotational quantum number  $N$ :  $B_{v'} N(N+1)$ , where  $B_{v'}$  was parametrized as  $B_e - \alpha_e(v'+1/2)$ .]

For a given level  $J$  of  ${}^6\Sigma^+$ , case (b) basis functions for rotational sublevels [according to the convention<sup>23,23</sup> that maximum  $J$  value corresponds to the level  $F_1(J_{\text{max}})$ ] are thus: (Ref. 24)  $F_1(N+5/2)$ ,  $F_2(N+3/2)$ ,  $F_3(N+1/2)$ ,  $F_4(N-1/2)$ ,  $F_5(N-3/2)$ ,  $F_6(N-5/2)$ . The rotating part of the molecule's basis set functions will then be (according to convention<sup>25</sup> of listing in order of decreasing energy at large  $N$ )

$$F_3(N+1/2) = |0^+, 5/2, N=J-1/2, J, M\rangle,$$

$$F_4(N-1/2) = |0^+, 5/2, N=J+1/2, J, M\rangle,$$

$$F_2(N+3/2) = |0^+, 5/2, N=J-3/2, J, M\rangle,$$

$$F_5(N-3/2) = |0^+, 5/2, N=J+3/2, J, M\rangle,$$

$$F_1(N+5/2) = |0^+, 5/2, N=J-5/2, J, M\rangle,$$

$$F_6(N-5/2) = |0^+, 5/2, N=J+5/2, J, M\rangle.$$

The  $e$  and  $f$  parity eigenfunctions are then generated as the sum and difference, respectively, of the  $N=J \pm n/2$  pair of basis functions.<sup>26,27</sup> Figure 1 shows these as an energy level diagram with the allowed transitions between them. Vibrational energy was approximated by the harmonic oscillator expression with mechanical anharmonicity added as the customary perturbation, through the  $\omega_e y_e$  term.

Since, in the higher resolution of the two spectra obtained, there appeared to be evidence of some resolution of rotational structure, it was considered important to have more precise line positions. Consequently, several additional perturbations to the energy were added. The high multiplicity of the term suggested that spin-coupling interactions should also be important. So, this coupling was included via the use of the dipolar spin-spin ( $\lambda$ ) and electron spin-rotation ( $\gamma$ ) coupling constants.

Analytic expressions for matrix elements were given in the work by Gordon and Merer.<sup>28</sup> These were used to set up a matrix representing the perturbing interactions of electron spin-spin and spin-rotation coupling, which was then numerically diagonalized to obtain perturbation energies for a given  $N$ , for each of its six  $J$  sublevels. The matrix and its elements are listed below:

$$\begin{bmatrix} \alpha(N-2, J) - E(N-2, J) & \beta(N, J) & 0 \\ \beta(N, J) & \alpha(N, J) - E(N, J) & \gamma(N, J) \\ 0 & \gamma(N, J) & \alpha(N+2, J) - E(N+2, J) \end{bmatrix},$$

where

$$\beta(N, J) = \frac{\lambda}{2} \sqrt{\frac{(N+J+\frac{5}{2})(N+J+\frac{7}{2})(N+J-\frac{5}{2})(N+J-\frac{7}{2})(N-J+\frac{3}{2})(N-J+\frac{5}{2})(J-N+\frac{7}{2})(J-N+\frac{9}{2})}{(2N-1)^2(2N+1)(2N-3)}}, \quad (5)$$

$$\gamma(N, J) = \beta(N + 2, J). \tag{6}$$

This gives, specifically,

$$J = N + \frac{5}{2}: \alpha(N, J) = \frac{-10\lambda}{3} \left( 1 - \frac{3}{2N+3} \right) + \frac{5}{2} \gamma N,$$

$$J = N + \frac{3}{2}: \alpha(N, J) = \frac{2\lambda}{3} \left( 1 + \frac{27}{2N+3} \right) + \frac{1}{2} \gamma(3N-5),$$

$$J = N + \frac{1}{2}: \alpha(N, J) = \frac{2\lambda}{3} \left( 4 + \frac{27}{2N+3} - \frac{15}{2N-1} \right) + \frac{1}{2} \gamma(N-8),$$

$$J = N - \frac{1}{2}: \alpha(N, J) = \frac{2\lambda}{3} \left( 4 - \frac{27}{2N-1} + \frac{15}{2N+3} \right) - \frac{1}{2} \gamma(N+9),$$

$$J = N - \frac{3}{2}: \alpha(N, J) = \frac{2\lambda}{3} \left( 1 - \frac{27}{2N-1} \right) - \frac{1}{2} \gamma(3N+8),$$

$$J = N - \frac{5}{2}: \alpha(N, J) = \frac{-10\lambda}{3} \left( 1 + \frac{3}{2N-1} \right) - \frac{5}{2} \gamma(N+1).$$

Accurately simulating the CL spectrum of the MnO  $A^6\Sigma^+ - X^6\Sigma^+$  transition was complicated by the commonly acknowledged perturbations in the upper electronic state. As Gordon and Merer said,<sup>28</sup> "... MnO provides an example of where just about all the problems that can occur in a diatomic molecule are present."

The transition moment was factored<sup>29-31</sup> into a product of the electronic transition moment, the vibronic band

strength (Franck-Condon factor or FCF)<sup>32</sup> and the rotational line strength (Hönl-London factor<sup>33</sup>). Rotational line strengths were calculated using the analytic expressions given in Kovács' monograph.<sup>34,35</sup> Having no information on the  $r$  dependence<sup>36</sup> of the electronic transition moment, we had to assume that it was the same for all the vibronic transitions. FCFs were obtained using rotationless, numerical Rydberg-Klein-Rees (RKR) potentials<sup>37</sup> for both the upper

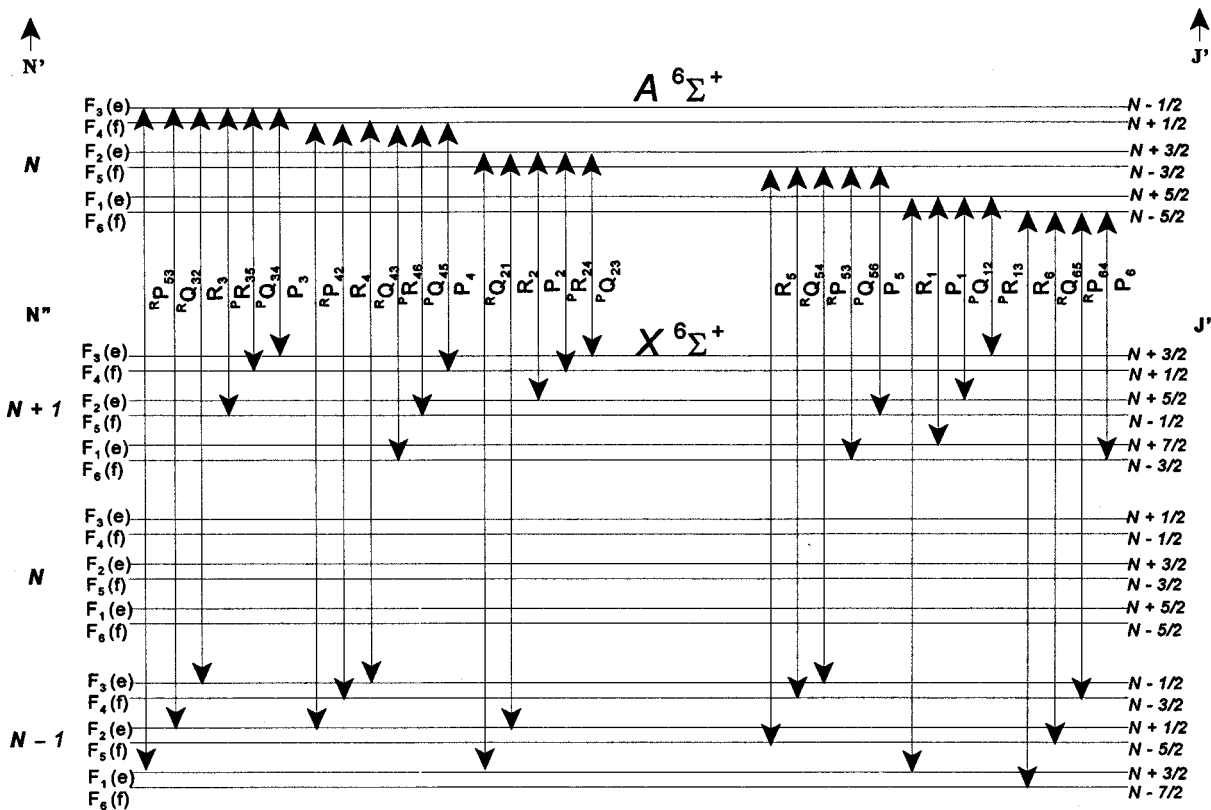


FIG. 1. Expected rotational transitions for Hund's case (b) MnO  $A^6\Sigma^+ - X^6\Sigma^+$ .

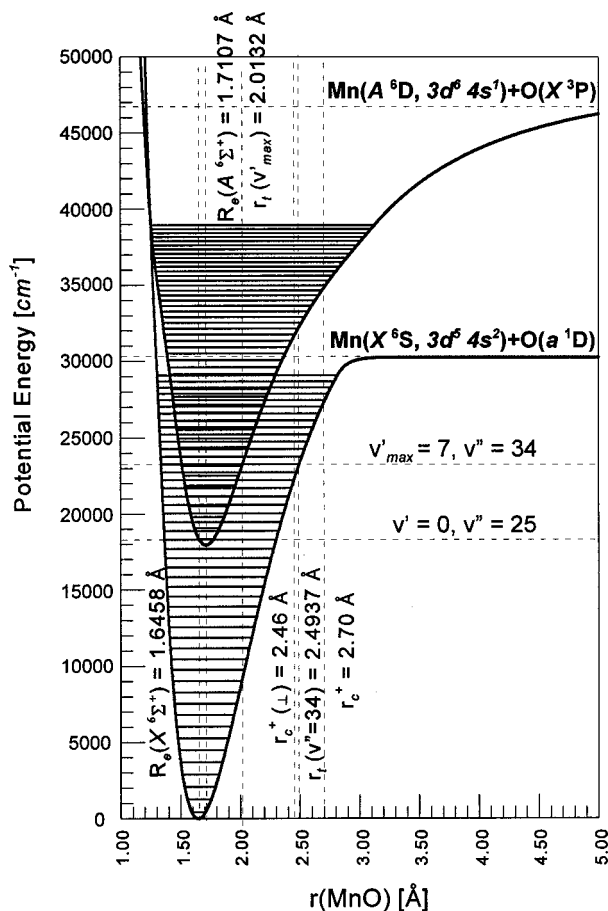


FIG. 2. Rotationless Klein–Dunham potential energy curves used to generate FCFs.

and lower electronic states (see Fig. 2). Energy constraints imposed on the simulation are given in Table II. Energy available for MnO was computed from the sum of the reaction exothermicity and the reactants' average relative translational and internal energies. The simulation did not use a reactant energy distribution as input.

The square of the difference between the experimental intensity and the theoretical intensity, normalized to the area

TABLE II. Energy constraints imposed on the spectral fit of Mn+O<sub>3</sub>.

Parameter	Values		
	[eV]	[cm <sup>-1</sup> ]	[K]
$D_0^0(\text{O}_2\text{-O})$	1.05 <sup>a</sup>		
$D_0^0(\text{X } ^6\Sigma^+ \text{ Mn-O})$	3.82 <sup>b</sup>		
$-\Delta H_0^0$	2.77		
$T_{\text{ozone}}$			293
$T_{\text{Mn}}$			1253
$E_{\text{trans}}$		773.6 <sup>c</sup>	
$E_{\text{rot,ozone}}$		305.5	
$E_{\text{vib,ozone}}$		0 <sup>d</sup>	

<sup>a</sup>Reference 85.

<sup>b</sup>Reference 83.

<sup>c</sup>The relative translational energy of the reactants was calculated as  $E_{\text{trans}} = (3/2)k_B T_{\text{effective}}$  where  $T_{\text{effective}} = (m_{\text{Mn}}T_{\text{O}_3} + m_{\text{O}_3}T_{\text{Mn}})/m_{\text{total}}$ .

<sup>d</sup>Vibrational excitation of ozone was neglected because less than 5% of the molecules were excited.

of the experimental spectrum, at each binned wavelength is summed over all binned wavelengths in the full experimental spectrum and minimized. It is the square root of this normalized sum of squares, i.e., chi-squared with uniform error, that is used as the figure of merit function to assess goodness of fit. Four adjustable parameters used to represent the vibrational and rotational distributions are described in Sec. IV. The LMDIF family of subroutines,<sup>38</sup> from the public domain nonlinear fitting package MINPACK,<sup>15</sup> was used to implement the minimization. This subset uses the Levenberg–Marquardt method to search for the minimum. More details are given elsewhere.<sup>39</sup>

Once the equations describing the populations are specified, i.e., the best-fit values have been found, the deviation from the statistical (Prior) population, i.e., the Surprisal, can be determined, using information theory.<sup>40–44</sup> The Prior population for  $M, J$  states in one of two diatomic molecules formed in an atom–triatom reaction is proportional to  $E_{\text{trans}}^{5/2}$ .

#### IV. RESULTS

Spectra at two different resolutions were used—5.5 and 1.1 Å effective bandwidth. In the following discussion, the spectra taken with the 300 lines/mm grating and 0.125 mm entrance slit will be referred to as “low” resolution (5.5 Å effective bandwidth). In contrast, those taken with the 1200 lines/mm grating and 0.100 mm entrance slit (1.1 Å effective bandwidth) are “high” resolution. The spectra resulting from ozone reactions of Mn at the low-resolution best-fit values and those predicted from the Prior populations are shown in Fig. 3 (low resolution) and Fig. 4 (high resolution).

Both spectra were fitted individually to get best-fit parameters. The two sets of best-fit parameters were significantly different. The low-resolution parameters gave the better fits when used to fit both the low- and high-resolution spectra than did those obtained from the fit of the high-resolution spectrum. In the following discussion, “best-fit spectra” refers to those spectra obtained using the low-resolution best-fit parameter values. This implies that to obtain the most accurate fit it is necessary to include more than one vibronic sequence in the spectral region scanned.

Although the best-fit spectrum generally reproduces the main features of the experimental spectrum (whose rough profile agrees with that established in the spectroscopic works of Das Sarma<sup>45</sup> and Joshi<sup>46</sup>), it is readily observed that, unlike the experimental, the simulated spectrum has somewhat pronounced heads near the 0–0 and 0–1 band origins. A plot of the significant energy normalized FCFs against the experimental spectrum (see Fig. 3) demonstrates that no other significant vibronic transitions are expected in these regions.

We attribute this disagreement to the fact that we are attempting to use spectroscopic constants to model the entire spectrum. It is well-known that the  $v' = 0$  level of MnO  $A \ ^6\Sigma^+$  is significantly perturbed.<sup>28</sup> The principal perturbation is ascribed to a high vibrational level ( $v'' \approx 25$ ) of the ground electronic state and is close to Hund's case (b). One thought would be to model the CL using two electronic states as the upper state, the  $A \ ^6\Sigma^+$  state and the perturbing

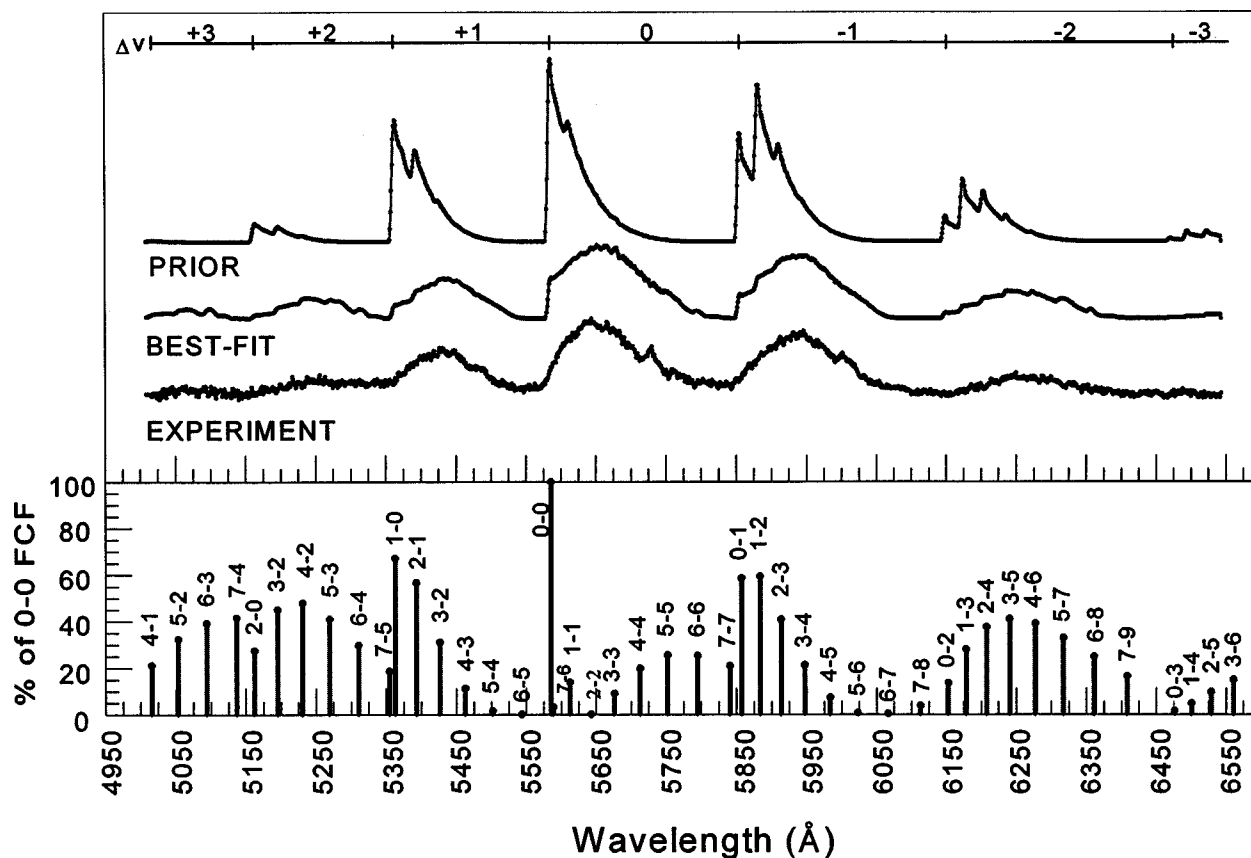


FIG. 3. Upper panel: low-resolution CL spectra—Prior (upper), best-fit (middle), and experimental (lower); lower panel: energy-normalized FCFs.

higher vibrational levels of  $X^6\Sigma^+$ . However, upon closer examinations, one realizes that this would only allow further degradation to the red, and not to the blue as needed. Consequently, we chose to ignore this discrepancy between simulated and experimental spectra.

The main new features evident in the high-resolution experimental spectrum are the appearance of two sharp peaks (around 5666.6 and 5730.0 Å). None of the fits was able to reproduce the position of these two peaks. Initially, it was thought that they might be due to a selective enhancement of a specific rotational or vibrational transition. A comparison of the experimental spectrum against the energy-normalized FCFs (see Fig. 4) demonstrated that no band heads were found to be very near to these positions. However, closer inspection of the experimental spectrum shows, in places, a doubling which appears to smoothly vary in separation with wavelength. This suggests to us that the two sharp peaks probably arise from constructive interference of the overlapping  $P$  and  $R$  branches in the band, i.e., as the contribution from each branch comes in and out of phase, and so cannot be attributed to any two specific rotational transitions (see Fig. 5).

We have obtained two different sets of populations, using the low- and high-resolution spectra. For reasons indicated earlier, the populations reported here are those from the low-resolution spectrum. The vibrational populations and the Surprisal plots are shown in Fig. 6. The rotational populations and their respective Surprisals obtained for  $v'=0$  are shown in Fig. 7. Best-fit parameters for the low-resolution

spectrum are presented in Table III. Populations are built on the Prior distributions and parametrized as follows:

$$P(v', N') = P^o(v', N') \exp(\lambda_{\text{rot}_1} g_{N', v'} + \lambda_{\text{rot}_2} g_{N', v'}^2), \quad (7)$$

$$P(v') = P^o(v') \exp(\lambda_{\text{vib}_1} f_{v'} + \lambda_{\text{vib}_2} f_{v'}^2), \quad (8)$$

where  $P^o(v', N')$  and  $P^o(v')$  are the Prior distributions in the upper state. From the simulations, it is seen that the nascent product is rotationally hot compared to the Prior distributions, but not vibrationally hotter.

Results of the TOF measurements are shown in Fig. 8. The experimental points are compared to the best-fit simulation based on a collision-energy dependence of the cross section presented by Gonzalez Ureña,<sup>47,48</sup> which he attributes to a microcanonical transition state theory (MTST)

$$\sigma = c \frac{(E - V_0)^n}{E}. \quad (9)$$

The barrier  $V_0$  from the fit was 0.364 kJ mol<sup>-1</sup>, and the exponent  $n$  was 0.709. A somewhat poorer fit was obtained using  $\sigma$  proportional to  $E^n$ , and in that case the exponent  $n$  was  $-0.239$ . Figure 9 compares these two forms for the cross section, and shows that their shapes are nearly the same over the region of collision energy to which the experiment was sensitive.

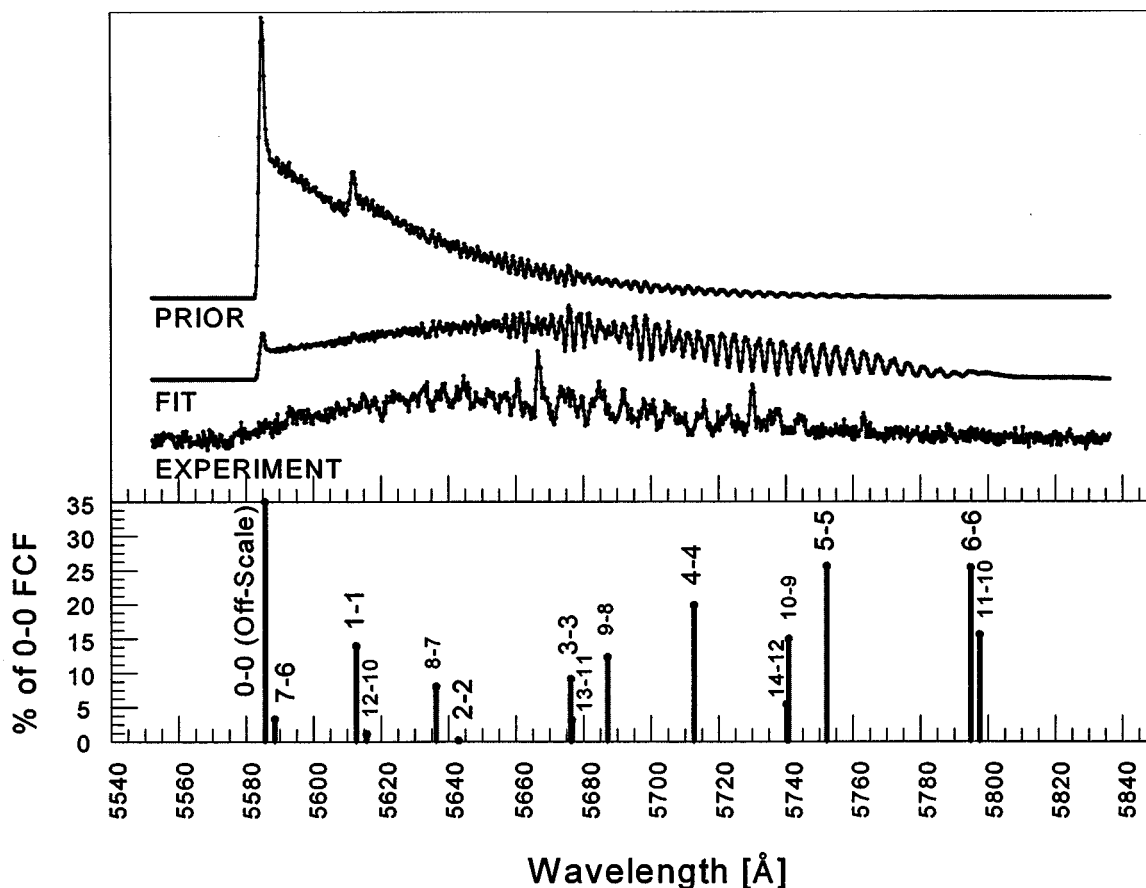


FIG. 4. Upper panel: high-resolution CL spectra—Prior (upper), fit at low-resolution best-fit values (middle), and experimental (lower); lower panel: energy-normalized FCFs.

## V. DISCUSSION

Since the results for energy disposal in MnO display marked deviations from the Prior model expectations, we look to kinematic or dynamic constraints as possible causes. Kinematic constraints are dictated by the masses, velocities, and extent of a critical configuration that couples reactants and products. They may dominate when the departing group

is light relative to the atoms in the product molecule, i.e., a reaction of the type  $H+LH \rightarrow L+HH$ . Although the  $Mn+O_3 \rightarrow MnO+O_2$  reaction does not satisfy this mass criterion well, kinematics could still be important if dynamic constraints are weak. Dynamic effects arise in general from the actual electromagnetic interaction between the particles throughout the course of a collision. They will be important if the potential energy surface exhibits rapid energy changes, which can be thought of as providing impulsive forces on the particles that constrain the way energy is released into prod-

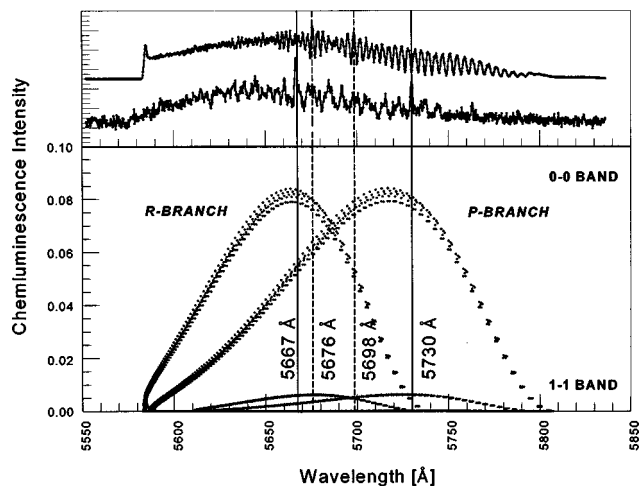


FIG. 5. MnO  $A^6\Sigma^+ - X^6\Sigma^+$  calculated rotational intensities for vibrational bands 0-0, 1-1. (All other vibrational transitions for  $\Delta v=0$  sequence are one to two orders of magnitude smaller.)

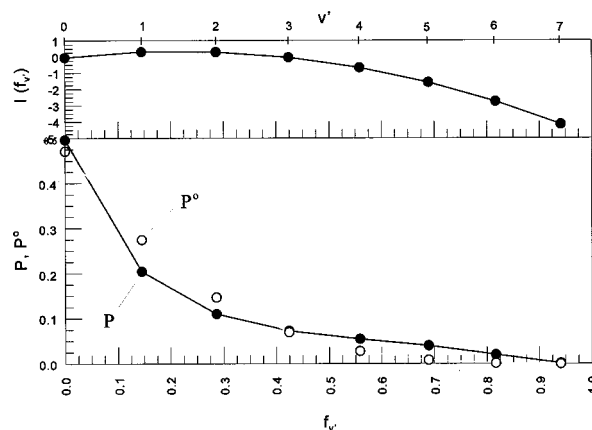


FIG. 6. Vibrational populations and Surprisal at low-resolution best-fit values.

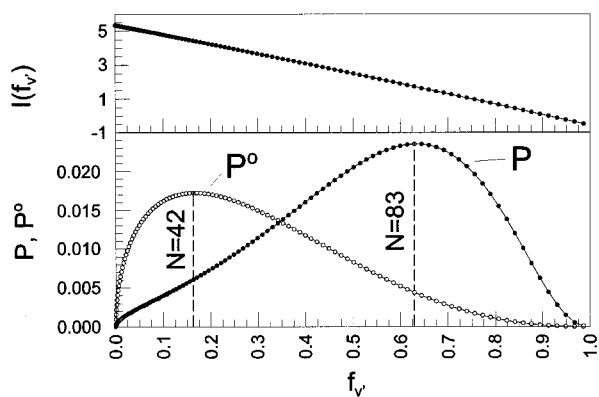


FIG. 7. Rovibrational populations and Surprisal at low-resolution best-fit values for  $v'=0$ .

ucts or required in reactants. A commonly cited sample is the harpoon mechanism, in which strong long-range Coulombic forces of attraction develop after the sudden electron jump from a metal atom, imposing an impulsive torque on the nascent anion.<sup>49</sup>

In considering whether strong impulses are to be expected here, we first review briefly what is known about the electronic structure of MnO and O<sub>3</sub>. Then, we consider the interaction in terms of molecular orbital populations and suggest that a long-range electron-transfer model is not appropriate. Finally, both kinematic and dynamic models will be used to estimate product MnO rotational excitation for comparison with the experimental results.

### A. Electronic structure of MnO

Transition metal complexes are most often described as having donor–acceptor bonding which is usually interpreted within the framework of the Dewar–Chatt–Duncanson (DCD) model.<sup>50,51</sup> The DCD model qualitatively rationalizes bonding in transition metal complexes in terms of forward  $\sigma$ -donation and  $\pi$ -backdonation of valence electrons. The  $\sigma$ -bonding electrons from the metal are principally  $sd^n$  hybridized.<sup>52,3</sup>

Figure 10 presents the MnO molecular orbital diagram, drawn to reflect current understanding.<sup>2,5,53–55</sup> Pinchemel and Schamps<sup>1,2</sup> assign  $A^6\Sigma^+ - X^6\Sigma^+$  as the chemiluminescent transition of MnO\*. They argue this is specifically due to the  $10\sigma^* \rightarrow 8\sigma$  charge-transfer de-excitation. The two electronic states involved in the spectroscopic transition adiabatically correlate at short range to the same single-configuration ionic states<sup>2</sup>

TABLE III. Best-fit values for the parameters in the product rotational and vibrational distributions.

Fitting parameter	Best-fit value
$\lambda_{\text{rot1}}$	5.468 939
$\lambda_{\text{rot2}}$	0.446 344 4
$\lambda_{\text{vib1}}$	-3.623 752
$\lambda_{\text{vib2}}$	8.484 378

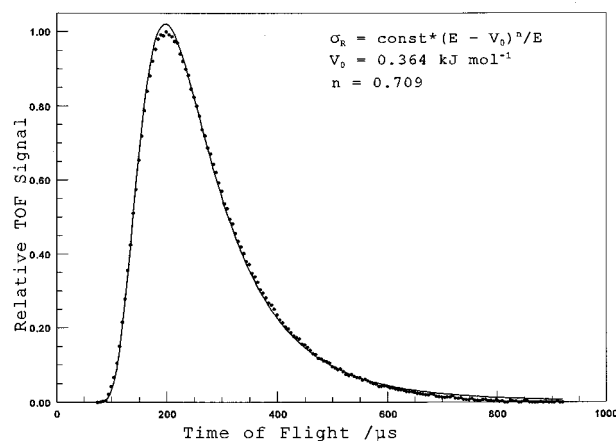
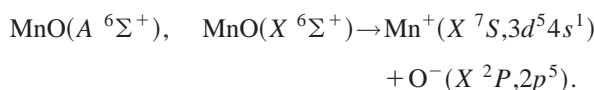
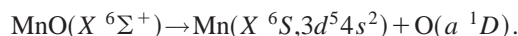
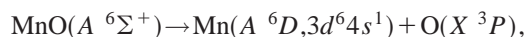


FIG. 8. Mn+O<sub>3</sub> TOF data fitted to an MTST cross section. The experimental data are shown by the filled circles.



They correlate at long range to the following single-configuration atomic states:<sup>2</sup>



Note that the  $A^6D$  state is not thermally accessible in this experiment. We can use this adiabatic correlation to infer that Mn will become increasingly  $sd_{z^2}$  hybridized as it approaches ozone. So, at short range, immediately preceding charge transfer, the Mn will resemble the  $A^6D$  atomic state. Indeed, Bauschlicher and Maitre, in their *ab initio* study,<sup>55</sup> find that the bonding in MnO  $X^6\Sigma^+$  is better represented by a two-configuration wave function that includes the contribution from the Mn  $A^6D$  state.

Recent analysis of experimental hyperfine coupling constants has demonstrated that in the  $X^6\Sigma^+$  state the  $4s$  and  $3d_{z^2}$  orbitals of Mn hybridize in approximately a 1:1 ratio,<sup>5</sup> and it is the  $sd_{z^2}$  hybrid ( $h_1$ ) that points in the direction of the O that combines in a bonding ( $8\sigma$ ) and antibonding fashion ( $10\sigma^*$ ). The other hybrid ( $h_2$ ) remains nonbonding, lo-

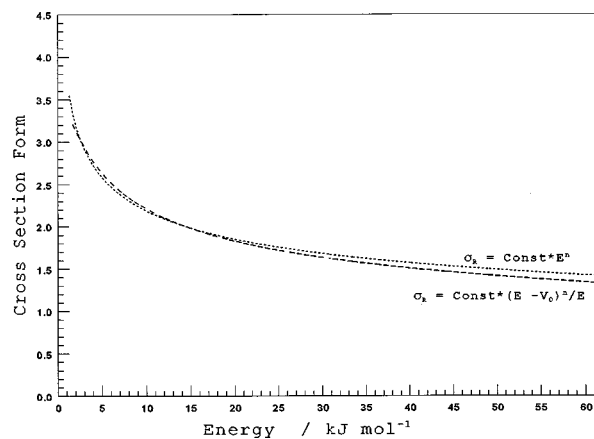
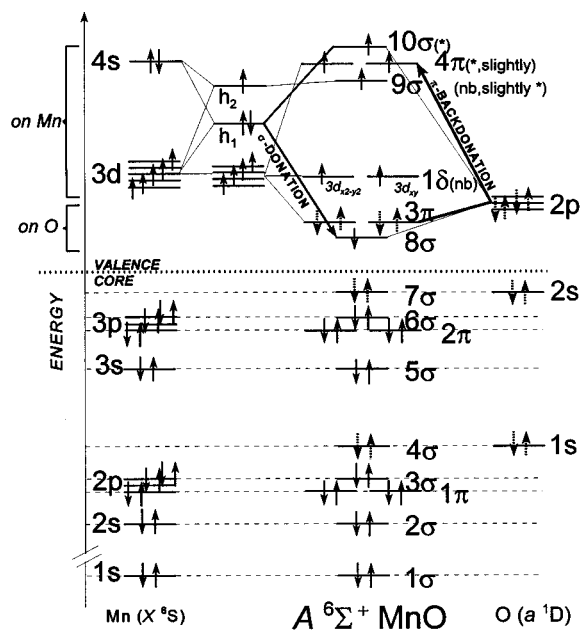


FIG. 9. Energy dependence of two forms of the cross section (MTST and  $E^n$ ) used to fit the TOF data over a time-delay range of 84–754  $\mu\text{s}$ .

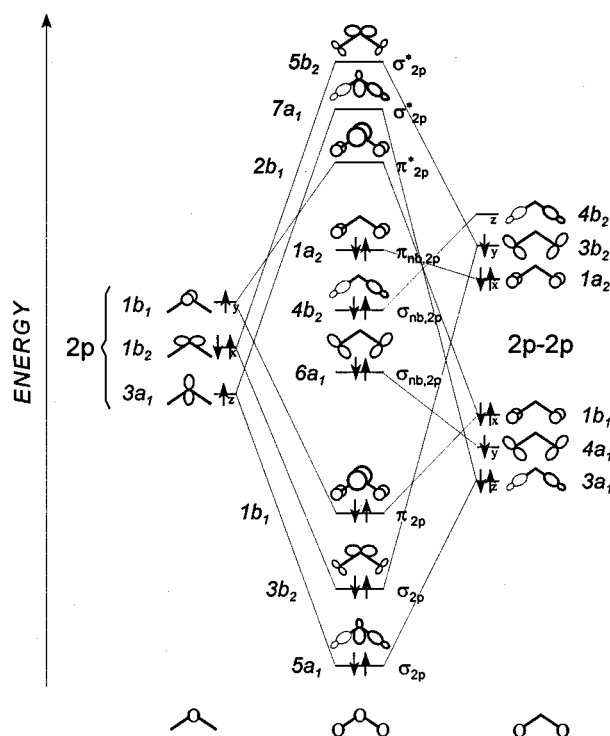
FIG. 10. Orbital correlation diagram for  $A^6\Sigma^+$  MnO.

calized on the Mn. In forming the MnO  $A^6\Sigma^+$  state, only one electron will be shifted from the Mn towards the O to give a singly occupied MnO  $8\sigma$  orbital. For the correlation of the Mn  $h_1$  to the MnO  $10\sigma^*$ , singly occupied in the  $A^6\Sigma^+$  state, a minimal movement of electron density is required because this molecular orbital (MO) resides largely on the Mn atom. No experimental dipole moment measurements are available to assess the ionic character of the bond, but theoretical values<sup>56</sup> do exist. It is important to recognize that accurate dipole moments for transition metal compounds are difficult to calculate. The most reliable level of theory for the metal oxides appears to be the unrestricted coupled-cluster calculation<sup>55</sup> with single-, double-, and some triple excitations included, UCCSD(T),<sup>55</sup> which gives 4.99 D for  $X^6\Sigma^+$  MnO. This is about 63% of the purely ionic value (7.899 D based on  $Mn^+-O^-$ ). Because the  $8\sigma \rightarrow 10\sigma^*$  excitation to form the  $A$  state moves electronic charge toward Mn, the  $A$  state bonding is predicted to be even less ionic.

## B. Electronic structure of $O_3$

Hay and Dunning<sup>57</sup> provide a state correlation diagram for  $O_3$  and  $O_2+O$ ; Bacis *et al.*<sup>58</sup> summarize the known dissociation limits for different electronic states of ozone. Figure 11 presents one possible, single-configuration correlation diagram<sup>59</sup> for the  $2p$  orbitals in  $C_{2v}$  ozone, drawn to reflect current understanding. (Note that it is well-known that the single-configuration approximation inadequately describes the ozone ground state,<sup>60</sup> but, for purposes of discussion, it is a useful starting point.) Orbitals not shown are generated from the  $1s$  and  $2s$  orbitals, i.e.,  $1a_1 1b_2 2a_1 3a_1 2b_2 4a_1$ .

There is disagreement in the literature about the relative energy ordering of valence MOs: both Tsuneda<sup>61</sup> and Arnold<sup>62</sup> give MO ordering as presented in the figure shown, but Borowski<sup>63</sup> gives the ozone  $1b_1$  as lower in energy than the  $3b_2$ , and also the  $4b_2$  before the  $6a_1$ . However, both

FIG. 11.  $O\ 2p(X^3P)-O_2\ 2p\pi(^3\Sigma_g^-)$  correlations in  $C_{2v}O_3(X^1A_1)$ , according to the fragment orbital method. (Only dominant interactions are shown.)

sides agree with identification of the  $\sigma$  or  $\pi$  nature of the molecular orbitals. Alcamí<sup>64</sup> gives a picture of the electron density contours of the ozone molecular orbitals in his paper.

## C. Evolution of electronic structure in the chemiluminescent $Mn+O_3$ reaction

To obtain maximal overlap between the ozone LUMO ( $2b_1$ ) and the manganese highest occupied molecular orbital (HOMO) ( $h_1$ ) requires that the Mn approach perpendicular to the ozone plane with the Mn  $3d\pi$ -orbitals coplanar with the  $2p\pi$  of its terminal oxygen, i.e., the O-O  $2p\sigma$  framework bonds.

Figure 12 shows the orbitals relevant to the discussion of the formation and subsequent de-excitation of  $MnO^*$ . That the  $MnO^*$  bond is largely covalent implies that  $O^-$  is not involved in the reaction and, consequently, that the anion of ozone is not formed in the  $Mn+O_3$  reaction. This is further substantiated by an estimate of the electron transfer distance using Magee's equation<sup>65,66</sup> with the assumption that no covalent interaction exists at that point. The vertical electron affinity for  $O_3$  is not available, and so we resort to using the experimental, adiabatic electron affinity of 2.103 eV.<sup>64,67</sup> Gonzalez-Luque<sup>68</sup> points out that the similar geometries of ground-state ozone and its negative ion should make the difference between the vertical and adiabatic electron affinities small. Using a Mn ionization energy 7.43 eV,<sup>69,70</sup> the estimated Mn- $O_3$  separation at the covalent-ionic crossing is 2.70 Å. This is only 1.58 times  $R_e$  for MnO  $A^6\Sigma^+$  (1.7107 Å). The actual distance of Mn to the nearest O atom in  $O_3$  depends, of course, on the direction of approach, but will be

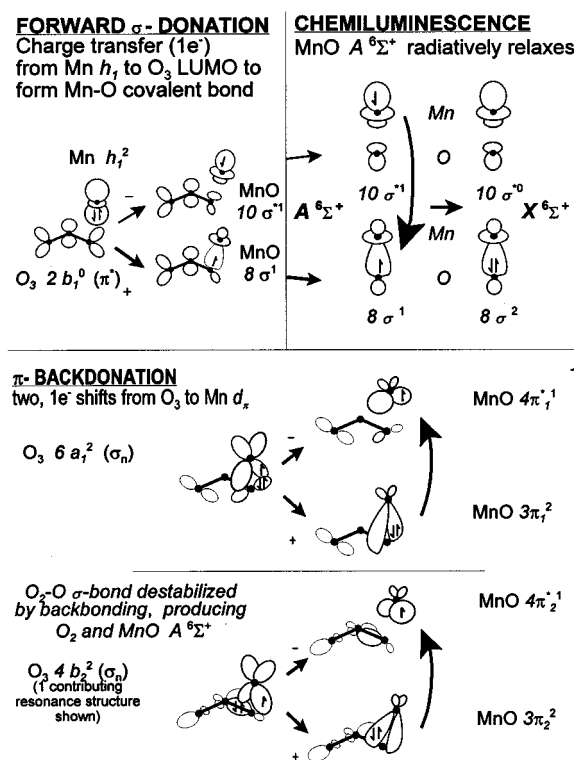


FIG. 12. Frontier orbital correlation for  $Mn + O_3 (X \ ^1A_1) \rightarrow MnO^* + O_2$ .

considerably less than 2.70 Å. At these short distances, covalent chemical bonding is already dominant in MnO. The TOF result that the cross section is rather weakly dependent on collision energy also indicates that no strong long-range attraction is present. The exponent of  $-0.239$  obtained in the power law fit could be associated with a rather short-range attractive potential. The estimated transfer distance of 2.70 Å falls in the intermediate range where adiabatic behavior is expected to dominate. If adiabaticity is assumed, then the orbitals of the reagents may be straightforwardly correlated to those of the products via symmetry. As noted earlier, Figs. 10 and 11 present orbital diagrams drawn to reflect current understanding of how the fragment orbitals correlate with their respective molecular products—MnO and  $O_3$ .

Figure 12 shows that the Mn's  $sd_{z^2}$ -hybrid that points in the direction of the O will overlap the electron cloud of ozone's terminal O. This orbital overlap produces a bonding orbital ( $8\sigma$ ) primarily centered on the O atom and an antibonding orbital ( $10\sigma^*$ ) principally centered on the Mn, according to well-known principles of molecular orbital theory.<sup>71</sup> We assume that the unobserved dioxygen product is in its ground electronic state  $X \ ^3\Sigma_g^-$  as has been justified by Zhang and Lee<sup>72</sup> for other reactions of ozone. In fact, there is insufficient energy to populate both the MnO A state and the lowest excited state of  $O_2$ ,  $a \ ^1\Delta_g$ .

It is possible that the electron could initially migrate to a two-center orbital yielding  $O_2^{\delta-}-O$  prior to  $O_2-O^{\delta-}$ . Two-center orbitals are often associated with complex insertion mechanisms as opposed to direct abstraction mechanisms for substitution reactions.<sup>73</sup> However, steric arguments suggest that initial interaction with a two-center  $O_3$  orbital is less

likely than with an orbital more localized on the terminal atom.

In donor-acceptor language, the new, polar-covalent Mn–O bond is strengthened by the strong forward  $\sigma$ -donation of one electron from the Mn  $h_1$  to the terminal O's  $2p\pi$ . This incipient Mn–O bond is further strengthened at the expense of the O–O bond by back donation from the terminal O's  $2p\sigma$  orbitals into the Mn  $3d\pi$  orbitals (MnO  $3\pi^*$ , centered on Mn).

The high rotational excitation of MnO which we have observed indicates that the mechanism is likely a direct one, as formation of a long-lived intermediate would be expected to lead much closer to statistical partitioning of product energy. Molecular beam studies by Lee and co-workers of ozone reactions with Na,<sup>74</sup> Ba,<sup>75</sup> and halogen atoms<sup>76</sup> have also demonstrated direct reactions, which appear to be dictated largely by the electronic structure of ozone.

We now consider how dynamic constraints operating in the chemiluminescent reaction channel might produce the rotationally hot products observed. Limiting possibilities are (i) sudden attractive energy release of energy as the reactants approach, and (ii) impulsive repulsive energy release as the products separate. The former does not seem appropriate because of the very close separations required to access ionic surfaces and the cold vibrational distribution observed in the MnO A state. The latter is the situation treated by the direct interaction with product repulsion (DIPR) model.<sup>66,77–79</sup> This model might be useful for estimating product energy disposal if  $O^- + O_2$  were suddenly formed on a repulsive surface, but the molecular orbitals involved in the chemiluminescent reaction channel clearly favor covalent bonding, i.e., partial, short-range charge transfer. Hence, the observed reaction is best characterized as following mixed release of energy, in which the forces of attraction and repulsion occur almost simultaneously without the occurrence of any distinct dynamic impulses.

The other result obtained by our experiments was the lack of vibrational excitation in the MnO\* product. Bourguignon *et al.*<sup>80</sup> have noted this same lack of vibrational excitation with significant rotational excitation in the  $Mg(^1S) + Cl_2$  reaction. They observed that short-range (although complete) charge transfer led to highly rotationally excited products because of a repulsive impulse in  $Cl_2^-$ . Had there also been strong long-range attraction of  $Mg^+$  to  $Cl_2^-$ , then high vibrational excitation would have been expected in MgCl. In the Mn+ $O_3$  reaction we have observed the same type of excited products for short-range *partial* charge transfer and suggest that the same dynamical effects are occurring.

Our mechanism allows dynamic repulsive forces to arise from weakening of bonding in  $O_3$  by backdonation from the  $4b_2$  molecular orbital. We can estimate an upper limit on the rotational excitation generated by repulsive release of energy in an  $O_2$ –O bond, assumed perpendicular to the Mn–O bond. A straightforward application of conservation of linear and angular momentum shows that 38.7% of this released energy will end up in rotation of MnO.<sup>39</sup> This corresponds to a rotational quantum number of 50, which is not as large as the most probable  $N$  of 83 found in the simulation of the

TABLE IV. Most probable rotational states ( $N^p$ ) for MnO  $A \Sigma^+$  in vibrational levels  $v$ , calculated using  $b_n = \text{HBL}(\text{MnO}^*) = 0.855 \text{ \AA}$ ,  $E_{\text{trans}} = 9.25 \text{ kJ mol}^{-1}$ ,  $v_{\text{rel}} = 850 \text{ m s}^{-1}$ , where  $N^p = \text{most probable } N$ .

$v$	Experimental				Calculated				
	$N^p$	$N^{p,\text{prior}}$	$N^{\text{max}}$	$T_e + E(v, N^p)$ ( $\text{cm}^{-1}$ )	$v^\perp$ ( $\text{m s}^{-1}$ )	$N^p$ ( $E_{\text{trans}}$ )	$T_e + E(v, N^p)$ ( $\text{cm}^{-1}$ )	% Error	% Expt
0	83	42	104	12 452.97	1981.6 850.0 <sup>a</sup>	68.4 29.3	20 475.31 18 731.71	-4.6 -12.7	95.4 87.3
1	77	39	97	21 031.00					
2	71	36	89	20 637.09					
3	64	32	80	20 214.03					
4	56	29	70	19 780.08					
5	47	24	59	19 356.83					
6	36	18	45	18 935.50					
7	20	10	25	18 516.23					

<sup>a</sup>No adjustment of the collision energy with the exothermicity, i.e.,  $v^\perp = v_{\text{rel}}$ .

experimental spectrum, but larger than the most probable  $N$  of 42 in the Prior distribution.

We are then led to explore the kinematics as a possible source of rotational energy in the MnO. In the kinematic limit, the products' rotational distributions are determined by both the distribution of the reactive impact parameters and also the initial rotational distributions of the reactants.<sup>81</sup> What is apparent is that the symmetry-favored collision pathway (nonplanar approach of Mn toward an end O) has a large impact parameter. Consequently, as has been previously noted by Lee *et al.* for ozone reactions with atomic chlorine<sup>72</sup> and bromine,<sup>76</sup> a large amount of the translational energy is expected to be converted into the rotational energy of the intermediate due to kinematics alone.

To determine if it is the kinematics that mainly causes the observed product rotation, we have calculated the level of rotational excitation predicted by a purely kinematic model—specifically, McCaffery's quantum-constrained-kinematic model.<sup>81</sup> This model is the extension of that group's angular momentum model for rotational energy transfer to reactive scattering. It focuses on the conversion of relative reactant linear momentum to diatomic product rotational angular momentum and/or scattered recoil momentum via a torque arm ( $b_n$ ), which can be approximated by half the bond length of the nascent product (HBL). It is through this rotor arm that the influence of the intermolecular potential is brought into the model. (The bond length usually signals the boundary of the potential's repulsive wall.) The simple equation for  $\text{Mn} + \text{O}_3 \rightarrow \text{MnO} (A \ ^6\Sigma^+) + \text{O}_2$  is

$$N^p = \mu_{\text{Mn},\text{O}_3} v_{\text{rel}}^p b_{n,\text{MnO}}^p \quad (10)$$

where  $N^p$  is the most probable value of  $N$ . The most probable relative velocity,  $v_{\text{rel}}^p$ , is defined as the component ( $v^\perp$ ) of the total relative velocity ( $v_{\text{rel}}$ ) perpendicular to the bond to be broken in the reaction. The average relative translational energy shown in Table II gives  $850.0 \text{ m s}^{-1}$  for the average relative velocity of Mn and ozone under our experimental conditions. McCaffery also computes an adjusted relative velocity from the average collision energy—adjusted to take into account the exothermicity and electronic energy. He does so by substituting ( $E_{\text{trans}} - \Delta H_{rxn} - T_e$ ) for  $\bar{E}_{\text{trans}}$  in

calculating the relative velocity. Adjusting the collision energy by the reaction exothermicity and electronic energy corresponds to assuming that all the exoergicity is converted into momentum along that one coordinate used to reach the reaction geometry. Consequently, it is an extreme case that for exoergic reactions overestimates the momentum in that coordinate and so represents an upper limit to the most probable rotational quantum number. Actually, McCaffery's model is imposing dynamic constraints for both the cases of the unadjusted and the adjusted collision energy—it is not a purely kinematic model. In either case, the choice of the HBL for the effective impact parameter is a choice of dynamic constraint. Moreover, in the adjusted case, when the excess energy is assumed to be completely converted into momentum of the reactants, this is an additional dynamic constraint. The adjusted limiting case represents an extreme limiting case, as repulsive interactions between the reactants' electron clouds would be expected to slow down the reactants before they reach hard-sphere distances. Applying McCaffery's quantum-constrained-kinematic model to the  $\text{Mn} + \text{O}_3$  system for  $v' = 0$  (see Table IV), we have predicted the most probable rotational quantum number (calculated  $N^p$ ) and compared this value to those obtained from the fit (experimental  $N^p$ ). Two different values for the most probable rotational quantum number were computed: one from the collision energy itself ( $N^p = 29$ ), and the other from the collision energy adjusted by the reaction exoergicity ( $N^p = 68$ ). Both are lower than the experimental result.

## VI. CONCLUSIONS

The observed formation of MnO in its  $A \ ^6\Sigma^+$  state in the reaction of Mn with  $\text{O}_3$  is understandable by correlating atomic and molecular orbitals adiabatically. It is vibrationally cold but rotationally hot. The low vibrational energy content and weak collision-energy dependence of the cross section indicate that there is no strong attraction or repulsion as the reactants approach. The high rotational energy content appears to arise partially from kinematics but also from repulsive release of energy along an  $\text{O}_2\text{--O}$  direction which is perpendicular to the Mn–O bond.

## ACKNOWLEDGMENTS

The authors thank Navin Rajagopalan and John Evans for their assistance in carrying out the experiments. Support of the National Science Foundation is gratefully acknowledged.

- <sup>1</sup>B. Pinchemel and J. Schamps, *Can. J. Phys.* **53**, 431 (1975).
- <sup>2</sup>B. Pinchemel and J. Schamps, *Chem. Phys.* **18**, 481 (1976).
- <sup>3</sup>L. E. Orgel, *J. Chem. Soc.* **1958**, 4186.
- <sup>4</sup>R. F. Ferrante *et al.*, *J. Chem. Phys.* **67**, 5904 (1977).
- <sup>5</sup>K.-I. Namiki and S. Saito, *J. Chem. Phys.* **107**, 8848 (1997).
- <sup>6</sup>R. Woodward, P. N. Le, M. Temmen, and J. L. Gole, *J. Phys. Chem.* **91**, 2637 (1987).
- <sup>7</sup>T. C. Devore, J. R. Woodward, and J. L. Gole, *J. Phys. Chem.* **93**, 4920 (1989).
- <sup>8</sup>M. R. Levy, *J. Phys. Chem.* **93**, 5195 (1989).
- <sup>9</sup>M. R. Levy, *J. Phys. Chem.* **95**, 8500 (1991).
- <sup>10</sup>M. A. Spence and M. R. Levy, *J. Phys. Chem. A* **101**, 7490 (1997).
- <sup>11</sup>B.-S. Cheong, M. D. Oberlander, R. P. Kampf, and J. M. Parson, *J. Chem. Phys.* **99**, 5104 (1993), and references therein.
- <sup>12</sup>R. P. Kampf and J. M. Parson, *J. Chem. Phys.* **108**, 7595 (1998).
- <sup>13</sup>W. E. Blass, *Appl. Spectrosc. Rev.* **11**, 57 (1976).
- <sup>14</sup>P. Pelikán, M. Ceppan, and M. Liška, *Applications of Numerical Methods in Molecular Spectroscopy* (CRC Press, Boca Raton, 1993), Chap. 1.
- <sup>15</sup>ABSTRACT: MINPACK-1 Subroutine Library (#3722001), *Nonlinear Minimization Package* (Argonne National Laboratory, Argonne, IL, 1986). Available at: <http://www.iuc.edu/depts/adn/infwww/txt/v3722001.txt>
- <sup>16</sup>L. Pasternak and P. J. Dagdigian, *J. Chem. Phys.* **67**, 3854 (1977).
- <sup>17</sup>E. U. Condon and G. H. Shortley, *The Theory of Atomic Spectra* (MacMillan, New York, 1935).
- <sup>18</sup>D. M. Manos and J. M. Parson, *J. Chem. Phys.* **63**, 3575 (1975).
- <sup>19</sup>J. B. Tatum, *Astrophys. J., Suppl.* **14**, 21 (1966).
- <sup>20</sup>B. R. Frieden, *Probability, Statistical Optics, and Data Testing: A Problem Solving Approach*, 2nd ed. (Springer Series in Information Science 10, Springer, New York, 1991), Chap. 2.
- <sup>21</sup>B.-S. Cheong and J. M. Parson, *J. Chem. Phys.* **100**, 2637 (1994).
- <sup>22</sup>A. Gonzalez Ureña and R. Vetter, *Int. Rev. Phys. Chem.* **15**, 375 (1996).
- <sup>23</sup>R. N. Zare, *Angular Momentum: Understanding Spatial Aspects in Chemistry and Physics* (Wiley-Interscience, New York, 1988), Section 6.5.
- <sup>24</sup>B. Klemm and U. Uhler, *Can. J. Phys.* **37**, 537 (1959).
- <sup>25</sup>P. F. Bernath, *Spectra of Atoms and Molecules* (Oxford University, New York, 1995), p. 318.
- <sup>26</sup>J. M. Brown *et al.*, *J. Mol. Spectrosc.* **55**, 500 (1975).
- <sup>27</sup>P. R. Bunker and P. Jensen, *Molecular Symmetry and Spectroscopy*, 2nd ed. (National Research Council, Ottawa, 1998).
- <sup>28</sup>R. M. Gordon and A. J. Merer, *Can. J. Phys.* **58**, 642 (1980).
- <sup>29</sup>A. Schadee, *J. Quant. Spectrosc. Radiat. Transf.* **7**, 169 (1967).
- <sup>30</sup>E. E. Whiting and R. W. Nicholls, *Astrophys. J., Suppl.* **235**, 1 (1974).
- <sup>31</sup>E. E. Whiting *et al.*, *J. Mol. Spectrosc.* **80**, 249 (1980).
- <sup>32</sup>A. Schadee, *J. Quant. Spectrosc. Radiat. Transf.* **19**, 451 (1978).
- <sup>33</sup>R. N. Zare, *Angular Momentum: Understanding Spatial Aspects in Chemistry and Physics* (Wiley-Interscience, New York, 1988), p. 313.
- <sup>34</sup>I. Kovács, *Spectra of Diatomic Molecules* (American Elsevier, New York, 1969).
- <sup>35</sup>E. E. Whiting, J. A. Paterson, I. Kovács, and R. W. Nicholls, *J. Mol. Spectrosc.* **47**, 84 (1973).
- <sup>36</sup>C. Noda and R. N. Zare, *J. Mol. Spectrosc.* **95**, 254 (1982).
- <sup>37</sup>A. L. G. Rees, *Proc. Phys. Soc. London* **59**, 998 (1947).
- <sup>38</sup>B. S. Garbow, K. E. Hillstom, and J. J. Moré, *Documentation for MINPACK Subroutine LMDIF, Double Precision Version* (Argonne National Laboratory, Argonne, IL, 1980). Available at: <http://www.tu-berlin.de/zr/software/numerik/minpack/lmdif.txt>
- <sup>39</sup>K. M. Green, M. S. thesis, The Ohio State University, 1999.
- <sup>40</sup>R. B. Bernstein and R. D. Levine, *J. Chem. Phys.* **57**, 434 (1972).
- <sup>41</sup>R. D. Levine and R. B. Bernstein, *Faraday Discuss. Chem. Soc.* **55**, 100 (1973).
- <sup>42</sup>R. B. Bernstein and R. D. Levine, *Adv. At. Mol. Phys.* **11**, 215 (1975).
- <sup>43</sup>R. D. Levine, *Annu. Rev. Phys. Chem.* **29**, 59 (1978).
- <sup>44</sup>R. D. Levine and J. L. Kinsey, in *Atom-Molecule Collision Theory: A Guide for the Experimentalist*, edited by R. B. Bernstein (Plenum, New York, 1979), Chap. 22.
- <sup>45</sup>J. M. Das Sarma, *Z. Phys.* **157**, 98 (1959).
- <sup>46</sup>K. C. Joshi, *Spectrochim. Acta* **18**, 625 (1962).
- <sup>47</sup>A. Gonzalez Ureña, *Mol. Phys.* **52**, 1145 (1984).
- <sup>48</sup>A. Gonzalez Ureña, *Adv. Chem. Phys.* **66**, 213 (1987).
- <sup>49</sup>I. R. Elsum and R. G. Gordon, *J. Chem. Phys.* **76**, 3009 (1982).
- <sup>50</sup>J. S. Dewar, *Bull. Soc. Chim. Fr.* **1951**, C71.
- <sup>51</sup>J. Chatt and L. A. Duncanson, *J. Chem. Soc.* **3**, 2939 (1953).
- <sup>52</sup>G. Frenking and U. Pidun, *J. Chem. Soc. Dalton Trans.* **10**, 1653 (1997).
- <sup>53</sup>A. J. Merer, *Annu. Rev. Phys. Chem.* **40**, 407 (1989).
- <sup>54</sup>E. G. Bakalbassis *et al.*, *Chem. Phys.* **205**, 389 (1996).
- <sup>55</sup>C. W. Bauschlicher, Jr. and P. Maitre, *Theor. Chim. Acta* **90**, 189 (1995).
- <sup>56</sup>A. Szabo and N. S. Ostlund, *Modern Quantum Chemistry: Introduction to Advanced Electronic Structure Theory* (Dover, Mineola, NY, 1982).
- <sup>57</sup>P. J. Hay and T. H. Dunning, Jr., *J. Chem. Phys.* **67**, 2290 (1977).
- <sup>58</sup>R. Bacis, A. J. Bouvier, and J. M. Flaud, *Spectrochim. Acta A* **54**, 17 (1998).
- <sup>59</sup>E. E. Nikitin and S. Ya. Umanskii, *Theory of Slow Atomic Collisions* (Springer, New York, 1984), Section 3.3.
- <sup>60</sup>M. V. Rama Krishna and K. D. Jordan, *Chem. Phys.* **115**, 423 (1987).
- <sup>61</sup>T. Tsuneda, H. Nakano, and K. Hirao, *J. Chem. Phys.* **103**, 6520 (1995).
- <sup>62</sup>D. W. Arnold *et al.*, *J. Chem. Phys.* **101**, 912 (1994).
- <sup>63</sup>P. Borowski *et al.*, *J. Chem. Phys.* **103**, 266 (1995).
- <sup>64</sup>M. Alcamí *et al.*, *J. Chem. Phys.* **103**, 253 (1995).
- <sup>65</sup>J. L. Magee, *J. Chem. Phys.* **8**, 687 (1940).
- <sup>66</sup>M. G. Prisant, C. T. Rettner, and R. N. Zare, *J. Chem. Phys.* **81**, 2699 (1984).
- <sup>67</sup>S. E. Novick *et al.*, *J. Chem. Phys.* **70**, 2652 (1979).
- <sup>68</sup>R. Gonzalez-Luque *et al.*, *Theor. Chim. Acta* **86**, 467 (1993).
- <sup>69</sup>M. Dolg *et al.*, *J. Chem. Phys.* **86**, 866 (1987).
- <sup>70</sup>C. E. Moore, *Atomic Energy Levels as Derived from the Analyses of Optical Spectra* (National Bureau of Standards Circular 467, U.S. G. P. O., Washington, DC, 1952).
- <sup>71</sup>J. Yves, F. Volatron, and J. Burdett, *An Introduction to Molecular Orbitals* (Oxford University, New York, 1993), p. 81.
- <sup>72</sup>J. Zhang and Y. T. Lee, *J. Phys. Chem. A* **101**, 6458 (1997).
- <sup>73</sup>W. H. Breckenridge, *J. Phys. Chem. A* **100**, 14840 (1996).
- <sup>74</sup>M. H. Covinsky, A. G. Suits, H. F. Davis, and Y. T. Lee, *J. Chem. Phys.* **97**, 2515 (1992).
- <sup>75</sup>H. F. Davis *et al.*, *Ber. Bunsenges. Phys. Chem.* **94**, 1193 (1990).
- <sup>76</sup>J. Zhang, T.-T. Miao, and Y. T. Lee, *J. Phys. Chem. A* **101**, 6922 (1997).
- <sup>77</sup>P. J. Kuntz *et al.*, *J. Chem. Phys.* **44**, 1168 (1966).
- <sup>78</sup>P. J. Kuntz, E. M. Nemeth, and J. C. Polanyi, *J. Chem. Phys.* **50**, 4607 (1969).
- <sup>79</sup>P. J. Kuntz, E. M. Nemeth, and J. C. Polanyi, *J. Chem. Phys.* **50**, 4623 (1969).
- <sup>80</sup>B. Bourguignon *et al.*, *J. Phys. Chem.* **91**, 2080 (1987).
- <sup>81</sup>A. J. McCaffery, K. Truhins, and T. W. J. Whiteley, *J. Phys. B: At. Mol. Opt. Phys.* **31**, 2023 (1998).
- <sup>82</sup>K. P. Hüber and G. Herzberg, *Molecular Spectra and Molecular Structure. IV. Constants of Diatomic Molecules* (Van Nostrand Reinhold, New York, 1979).
- <sup>83</sup>S. Smoes and J. Drowart, *High Temp. Sci.* **17**, 31 (1984).
- <sup>84</sup>A. G. Adams, Y. Azuma, H. Li, A. J. Merer, and T. Chandrakumar, *Chem. Phys.* **152**, 391 (1991).
- <sup>85</sup>M. W. Chase, Jr., C. A. Davies, J. R. Downey, Jr., D. J. Frurip, R. A. McDonald, and A. N. Syverud, *J. Phys. Chem. Ref. Data* **14**, Suppl. 1, 1695 (1985).